Proceedings World Geothermal Congress 2020
Reykjavik, Iceland, April 26 – May 2, 2020

Inversion of Magnetic Data for Subsurface Temperature

Ketil Hokstad, Zuzana Alasonati Tašárová, Bjørn M. Sæther and Kati Tänavsuu-Milkeviciene

Equinor Research Centre, Arkitekt Ebbells vei 10, 7053 Trondheim, Norway

kehok@equinor.com

Keywords: exploration, magnetics, Bayesian inversion, IDDP-2

ABSTRACT

Rock magnetism and magnetic potential field data are influenced by many factors, including mineral composition, hydrothermal alteration, faults, and past and present temperatures. Laboratory measurements on rock samples from Reykjanes show that mid-oceanic ridge basalts possess large remanent magnetization and have two or three different Curie temperatures. This makes the inversion and interpretation of such data challenging.

We present a Bayesian inversion method for estimation of subsurface temperature from magnetic potential field data. The inversion is performed in two steps: First, we compute the magnetization, including both the induced and the remanent parts, by inversion of magnetic data. Due to the inherent ambiguity of potential field data, the depth resolution in the inversion is rather poor. This is why we use a Marquardt-Levenberg type map inversion method, computing laterally varying magnetization averaged over the relevant depth interval. Input to the inversion is total magnetic anomaly and magnetic background field, including inclination and declination. In young lavas, we assume that the paleomagnetic field at the time of lava eruption and solidification is approximately the same as the present-day field.

Second, we use a phenomenological model relating magnetization to temperature to perform inversion for subsurface temperature. The phenomenological model is based on spinodal exsolution of titanomagnetite and the Ising model from quantum statistics. The Ising model accounts for spin-spin interactions and interactions between spin and the external magnetic field. Therefore, it represents both the ferromagnetic and paramagnetic domain and reduces to the Currie-Weiss law in the high-temperature limit. The solid exsolution model describes the reorganization of initially homogeneous titanomagnetite into magnetite-rich and ulvöspinel-rich phases. The exsolution model is calibrated to laboratory measurements from the literature. The model is aimed at fast-cooled lavas with small or moderate oxidation of titanomagnetite.

The proposed Bayesian inversion scheme is demonstrated on high-resolution magnetic data acquired at Reykjanes, Southwest Iceland. Preliminary results indicate that lateral variations in subsurface temperature and hydrothermal alteration can be detected by the proposed inversion scheme. Inversion of magnetic data, like all geophysical data, gives ambiguous results. Therefore, the final aim and purpose of the proposed magnetic inversion are to include it as part of a multigeophysical inversion scheme, together with electromagnetic, seismic and gravity data.

1. INTRODUCTION

The magnetic properties of mid-oceanic ridge basalts have been studied extensively since the classical work of Vine et al (1963). They proposed that the alternating pattern of seabed lineaments with positive and negative magnetization was associated with sea floor spreading and reversals of the earth magnetic field. This complicates the analysis of rock magnetism for rocks that have experienced several flips of the magnetic field and tectonic movement away from the position of crystallization of the rock. Detailed analysis of the magnetic properties of old rocks requires estimates of both the paleomagnetic field and plate tectonic reconstructions to estimate the geographical origin of the rocks. Young basalts from places like Iceland are of special interest for magnetic studies, since these complications are less pronounced. Also, such investigations are of interest from a geothermal exploration point of view.

The magnetization of minerals and rocks can be seen as a battle between quantum-mechanical order and thermal disorder. The transition between these two domains take place around the Curie/Neel temperature. Below the Curie temperature the rock is ferromagnetic or ferrimagnetic. Above the Curie temperature, only a weak paramagnetism or diamagnetism remains. For this reason, we expect that magnetic data and magnetization may be a useful source of information about the presence of working geothermal systems.

The carriers of the magnetization of the mid-oceanic ridge basalts (MORB) are primarily titanomagnetite and secondarily titanomaghemite, the latter created by oxidation of the former. Titanomagnetite is known to be a solid solution of ulvöspinel and magnetite, formed when the basaltic lavas are cooled and solidified. Upon further cooling, the solid solution becomes unstable. Exsolution occurs when the titanomagnetite enters the miscibility gap of the phase diagram and leads to the decomposition of an initially homogeneous titanomagnetite into ulvöspinel-rich and magnetite-rich phases.

The exsolution can take place by two different mechanisms; spinodal and binodal exsolution. Spinodal exsolution is a diffusive process and is relatively fast. In laboratory experiments, this process runs within a few hours (Smith, 1980). Binodal exsolution is based on the formation of nuclei, and is associated with an energy barrier, in the form of an activation energy. Therefore, the binodal exsolution is slow (Wise et al., 2011), and operates on a much longer time scale (~Ma). JMAK kinetics can be applied to model binodal decomposition (Yund and McAlister, 1969; Farjas and Roura, 2006). In young MORB, it can be assumed that spinodal exsolution is the dominating mechanism. This is also supported by experimental studies (Wise et al., 2011).

Dietze et al. (2010) presented a study from the Reykjanes Peninsula, and concluded that titanomagnetite with small grain sizes is the main carrier of magnetization. They analyzed magnetic properties of rock samples, and related small-scale properties to magnetic potential field measurements. Laboratory measurements of susceptibility vs temperature show that two or sometimes three different Curie temperatures, between 30 ºC and 570 ºC can be found in each rock sample. Spinodal exsolution, and optionally oxidation of titanomagnetite, can explain why two or three Curie temperatures are observed. The Curie temperature depends on the Ti-fraction of the titanomagnetite, as presented by Lattard et al. (2006).

In the present paper, we present a two-step inversion scheme, similar to that of Hokstad et al. (2017) and Hokstad and Tänavsuu-Milkeviciene (2017). First, we use a simple and robust magnetic inversion scheme to compute the magnetization of the subsurface, including contributions from induced and remanent magnetization. Second, we develop a phenomenological model relating rock magnetization to temperature and rock composition, using a spinodal exsolution model, and a 1D Ising (1925) model. The phenomenological model is then used in a Bayesian inversion scheme, to invert rock magnetization for subsurface temperature. As a by-product of the inversion, we also obtain estimates of Curie temperatures and fractions of different titanomagnetite phases.

The proposed inversion methodology is demonstrated on densely sampled magnetic anomaly data from the Reykjanes Peninsula. In the Reykjanes field test, high-resolution magnetic data was acquired on foot, with a receiver elevation of 2.5 m above ground, and horizontal sampling interval of 12-13 m. For production-scale acquisition of magnetic data, we foresee the use of drones as a more practical method.

2. BAYESIAN INVERSION METHOD

Dependencies between physical quantities can conveniently be represented by Bayesian networks. Hokstad and Tänavsuu-Milkeviciene (2017) presented a general multigeophysical network for estimation of subsurface temperature for geothermal exploration (Figure 1a). Here we will investigate and expand on the magnetic branch of the network (Figure 1b). For this problem, the main parameters of interest are magnetic anomaly data B_A, rock magnetization M and subsurface temperature T. The meaning of other parameters shown in Figure 1b, is discussed later. In principle, all variables can be regarded as stochastic. Here we will use a simplified approach, taking only B_A, M and T as stochastic variables. The other are treated as deterministic parameters, or as having a delta-function distribution.

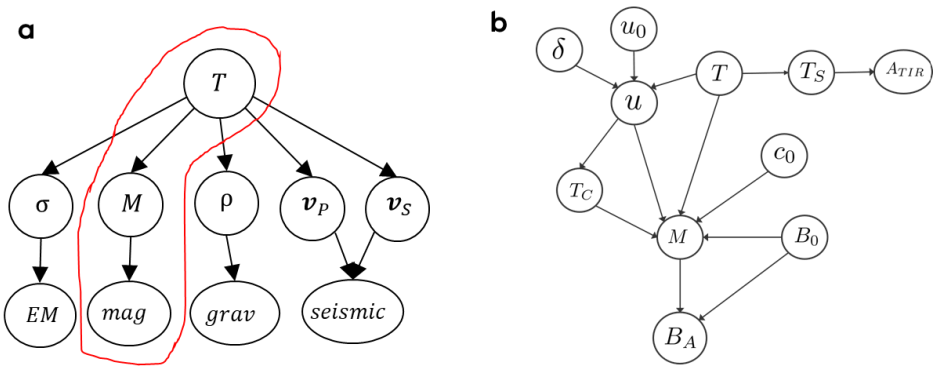

Figure 1: (a) Bayesian network for multigeophysical geothermal exploration presented by Hokstad and Tänavsuu-Milkeviciene (2017). (b) Bayesian network for estimation of subsurface temperature T from magnetic anomaly data B_A. T_S is surface temperature, A_{TIR} is the infrared bands from satellite data (e.g. LANDSAT-8), u_0 and u are initial and present-day fractions of ulvöspinel, δ represents the fraction of titanomagnetite oxidized to titanomaghemite, T_C is Curie temperature, B_0 is the earth magnetic background field (magnitude, inclination and declination), M is total rock magnetization (induced and remanent), and c_0 is the overall fraction of titanomagnetite in the basaltic rock.

The posterior distribution for subsurface temperature T given magnetic anomaly data B_A can be written as

$$p(T|B_A) = C \int dM\, p(T|M)p(M|B_A), \tag{1}$$

where C is the normalization factor, and M is the scalar magnitude of the magnetization. Given the posterior distribution in equation 1, magnetic anomaly data can (at least in theory) be inverted to obtain the mean and variance of the subsurface temperature. In practice, the inversion can be subdivided in two separate steps. First, we compute magnetization M by inversion of magnetic anomaly data B_A. Using Bayes rule, we obtain

$$p(M|B_A) \propto p(B_A|M)p(M). \tag{2}$$

This step is linear if we invert for magnetic properties constrained on geometry, which will be discussed in the next section. Second, we compute temperature T by inversion of magnetization M. Again, using Bayes rule, we obtain

$$p(T|M) \propto p(M|T)p(T). \tag{3}$$

The second inversion involves a non-linear phenomenological relationship between magnetization and temperature, which will be presented below. Finally, the posterior distribution $p(T|B_A)$ is obtained by means of Equation 1. When the first inversion step is linear, the marginalization of M can be written on convolution form, which allows for efficient computation using the fast Fourier transform (Buland et al., 2008). Given the posterior distribution, the mean and variance can be computed from their definitions.

3. MAGNETIC ANOMALY INVERSION

Magnetic anomaly data are due to dipole sources in the subsurface. The anomalous magnetic field $\mathbf{B_A}$ can be obtained by double differentiation of an inverse-distance potential (Blakely, 1996)

$$\mathbf{B_A}(\mathbf{x}) = -\frac{\mu_0}{4\pi}\nabla\nabla\cdot\int\frac{\mathbf{M}(\mathbf{x}')}{|\mathbf{x}'-\mathbf{x}|}\mathrm{d}V', \tag{4}$$

where $\mathbf{M}$ is the magnetization vector, $\mathbf{x}$' denotes the positions of magnetic sources, $\mathbf{x}$ are the positions where the magnetic field is measured, and μ_0 is the vacuum permeability. In standard acquisition of magnetic potential field data, only the magnitude of the total magnetic field, the total magnetic intensity, is measured,

$$\mathrm{B_{TMI}} = |\mathbf{B}_0 + \mathbf{B_A}| = \sqrt{|\mathbf{B}_0|^2 + |\mathbf{B_A}|^2 + 2\mathbf{B}_0\cdot\mathbf{B_A}}, \tag{5}$$

where $\mathbf{B}_0$ is the earth magnetic background field. The scalar total magnetic anomaly $\mathrm{B_A}$ is obtained by subtracting the magnitude of the local magnetic field, $\mathrm{B_A} = |\mathbf{B}_0 + \mathbf{B_A}| - |\mathbf{B}_0|$. Expanding the square-root to 2nd order in $\mathbf{B_A}$, the total magnetic anomaly can be written as

$$\mathrm{B_A} \simeq \mathbf{t}\cdot\mathbf{B_A} + \frac{|\mathbf{t}\times\mathbf{B_A}|^2}{|\mathbf{B}_0|}, \tag{6}$$

where $\mathbf{t} = \mathbf{B}_0/|\mathbf{B}_0|$ is a unit vector in the direction of $\mathbf{B}_0$. When $|\mathbf{B_A}| \ll |\mathbf{B}_0|$, the second term is insignificant, and the scalar magnetic field $\mathrm{B_A}$ is approximately the projection of the anomalous field onto the direction of the earth magnetic background field. This assumption is used in the following.

Magnetic data capture lateral changes in magnetization, but with limited depth resolution. Therefore, 3D magnetic inversion is severely ill-posed, and must be constrained to give meaningful results (e.g. Li and Oldenburg, 1996; Hokstad et al., 2017). The depth distribution of magnetic anomalies from 3D inversion is to a large degree controlled by the regularization used, and should not be over-interpreted. In the present work, we use a map-inversion method to circumvent this problem.

We assume that the magnetization vector is independent of depth, or it represents an average over the depth range $\mathrm{z_1}$ to $\mathrm{z_2}$, such that

$$\mathbf{M}(\mathrm{x},\mathrm{y}) = \frac{1}{\mathrm{z_2}-\mathrm{z_1}}\int_{\mathrm{z_1}}^{\mathrm{z_2}}\mathbf{M}(\mathrm{x},\mathrm{y},\mathrm{z})\,\mathrm{dz}. \tag{7}$$

Then the integral over z' in equation 4 can be carried out, giving

$$\int_{\mathrm{z_1}}^{\mathrm{z_2}}\frac{1}{\mathrm{r}}\mathrm{dz}' = \ln[(\mathrm{z}'-\mathrm{z})+\mathrm{r}]\,|_{\mathrm{z_1}}^{\mathrm{z_2}} = \mathrm{F}(\mathrm{z_2}) - \mathrm{F}(\mathrm{z_1}). \tag{8}$$

For later convenience, we have introduced the radial distance $\mathrm{r} = \sqrt{(\mathrm{x}'-\mathrm{x})^2 + (\mathrm{y}'-\mathrm{y})^2 + (\mathrm{z}'-\mathrm{z})^2}$, and the function

$$\mathrm{F}(\mathrm{z}') = \ln[(\mathrm{z}'-\mathrm{z})+\mathrm{r}]\,. \tag{9}$$

Substituting in equation 4, and using equation 8, the magnetic anomaly $\mathrm{B_A}$ can be written approximately as

$$\mathrm{B_A}(\mathbf{x}) \simeq \mathbf{t}\cdot\mathbf{B_A}(\mathbf{x}) = \frac{\mu_0}{4\pi}\sum_{\mathrm{i}=1}^{3}\sum_{\mathrm{j}=1}^{3}\int \mathrm{t_i}\mathrm{A_{ij}}(\mathbf{x},\mathbf{x}')\mathrm{M_j}(\mathrm{x}',\mathrm{y}')\mathrm{dx}'\mathrm{dy}'\,, \tag{10}$$

where $\mathrm{t_i}$ and $\mathrm{M_j}$ are elements of the vectors $\mathbf{t}$ and $\mathbf{M}$, respectively, and $\mathrm{A_{ij}}$ are the elements of a second-order tensor given by

$$\mathrm{A_{ij}} = \frac{\partial^2\mathrm{F}(\mathrm{z_2})}{\partial\mathrm{x_i}\,\partial\mathrm{x_j}} - \frac{\partial^2\mathrm{F}(\mathrm{z_1})}{\partial\mathrm{x_i}\,\partial\mathrm{x_j}}, \tag{11}$$

where

$$\frac{\partial^2\mathrm{F}(\mathrm{z}')}{\partial\mathrm{x_i}\,\partial\mathrm{x_j}} = -\frac{1}{[(\mathrm{z}'-\mathrm{z})+\mathrm{r}]^2}\left[\delta_{\mathrm{i3}} + \frac{(\mathrm{x_i}'-\mathrm{x_i})}{\mathrm{r}}\right]\left[\delta_{\mathrm{j3}} + \frac{(\mathrm{x_j}'-\mathrm{x_j})}{\mathrm{r}}\right] + \frac{1}{[(\mathrm{z}'-\mathrm{z})+\mathrm{r}]}\left[\frac{\delta_{\mathrm{ij}}}{\mathrm{r}} - \frac{(\mathrm{x_i}'-\mathrm{x_i})(\mathrm{x_j}'-\mathrm{x_j})}{\mathrm{r}^3}\right]. \tag{12}$$

The derivatives are with respect to coordinates $(\mathrm{x_1},\mathrm{x_2},\mathrm{x_3}) = (\mathrm{x},\mathrm{y},\mathrm{z})$, and δ_{ij} is the Kronecker delta function.

Equations 11 and 12 are equivalent to the results presented by Bhattacharyya (1964) (his equation 7). From equation 10, it's clear that three-component magnetization M cannot be readily obtained by inversion of scalar data $\mathrm{B_A}$. However, if the direction of magnetization is approximately known, we can try to invert for the magnitude, which is a feasible problem. Hence, we write $\mathbf{M} = \mathrm{M}\mathbf{e}$ where M and $\mathbf{e}$ are the magnitude and direction of the magnetization, respectively. For young igneous rocks, it is reasonable to assume $\mathbf{e} = \mathbf{t}$. It is difficult to distinguish remanent magnetization $\mathrm{M_R}$ from induced magnetization $\mathrm{M_I} = \chi\mathrm{H_0}$, where $\mathrm{H_0} = \mu_0\mathrm{B_0}$. Without additional information, the two parts are mixed together. In general, a tectonic reconstruction and kinematic restoration may be needed to estimate $\mathbf{e}$.

Assuming a magnetic inverse problem with n_d measurements and n_m model parameters, the forward model equation 10 can be rewritten on matrix-vector form as

$$\mathbf{d} = \mathbf{L}\mathbf{m} + \mathbf{n}, \tag{13}$$

where $\mathbf{d}$ is a dimension $n_d \times 1$ data vector with components $d_i = B_A(x_i, y_i, z_i)$, $\mathbf{m}$ is a $n_m \times 1$ model vector with components $m_j = M(x_j', y_j')$, $\mathbf{L}$ is a $n_d \times n_m$ matrix, and $\mathbf{n}$ is assumed to be Gaussian noise**.** When $\mathbf{e} = \mathbf{t}$, the elements of the matrix $\mathbf{L}$ becomes

$$L_{ij} = \frac{\mu_0}{4\pi}\sum_{k=1}^{3}\sum_{l=1}^{3} t_k A_{kl}(x_i, y_i, z_i, x_j', y_j')t_l\,. \tag{14}$$

In a statistical formulation of the inverse problem, using Bayes rule, the posterior distribution $p(\mathbf{m}|\mathbf{d})$ can be written as

$$p(\mathbf{m}|\mathbf{d}) = Cp(\mathbf{d}|\mathbf{m})p(\mathbf{m}) = Ce^{-\Phi}, \tag{15}$$

where C is a normalization factor, and Φ is the objective function for an optimization-type inverse problem,

$$\Phi = \frac{1}{2}[\mathbf{d} - \mathbf{L}\mathbf{m}]^T\boldsymbol{\Sigma}_d^{-1}[\mathbf{d} - \mathbf{L}\mathbf{m}] + \frac{1}{2}\mathbf{m}^T\boldsymbol{\Sigma}_m^{-1}\mathbf{m}. \tag{16}$$

The prior distribution for $\mathbf{m}$ is assumed to be Gaussian with zero mean, which is reasonable for inversion of anomaly data. Since the forward model equation 13 is linear in $\mathbf{m}$, the likelihood and posterior distributions are also Gaussian. Then maximizing the posterior probability is equivalent to minimizing the objective function Φ. This can be achieved with the least squares-pseudo inverse

$$\mu_{\mathbf{m}|\mathbf{d}} \simeq \mathbf{m} = \left[\mathbf{L}^T\boldsymbol{\Sigma}_d^{-1}\mathbf{L} + \boldsymbol{\Sigma}_m^{-1}\right]^{-1}\mathbf{L}^T\boldsymbol{\Sigma}_d^{-1}\mathbf{d}, \tag{17}$$

where $\mu_{\mathbf{m}|\mathbf{d}}$ denotes the posterior mean of the magnetization M. For simplicity, we choose $\boldsymbol{\Sigma}_d$ proportional to the identity matrix. Choosing the prior model covariance $\boldsymbol{\Sigma}_m$ as

$$\boldsymbol{\Sigma}_m^{-1} = \lambda\mathrm{diag}(\mathbf{L}^T\mathbf{L}), \tag{18}$$

the classical Marquardt-Levenberg solution is obtained, where, λ is a parameter controlling the relative weights of the data term and regularization term of the objective function.

The posterior covariance matrix is independent of the data, and can be written explicitly as (Anderson, T.W., 1994; Buland et al., 2008)

$$\boldsymbol{\Sigma}_{\mathbf{m}|\mathbf{d}} = \boldsymbol{\Sigma}_m - \boldsymbol{\Sigma}_m\mathbf{L}^T[\mathbf{L}\boldsymbol{\Sigma}_m\mathbf{L}^T + \boldsymbol{\Sigma}_d]^{-1}\mathbf{L}\boldsymbol{\Sigma}_m. \tag{19}$$

The posterior model variances are the diagonal elements of $\boldsymbol{\Sigma}_{\mathbf{m}|\mathbf{d}}$. The second term on the right-hand side is positive definite. Hence, the effect of adding information from data is to reduce the uncertainty.

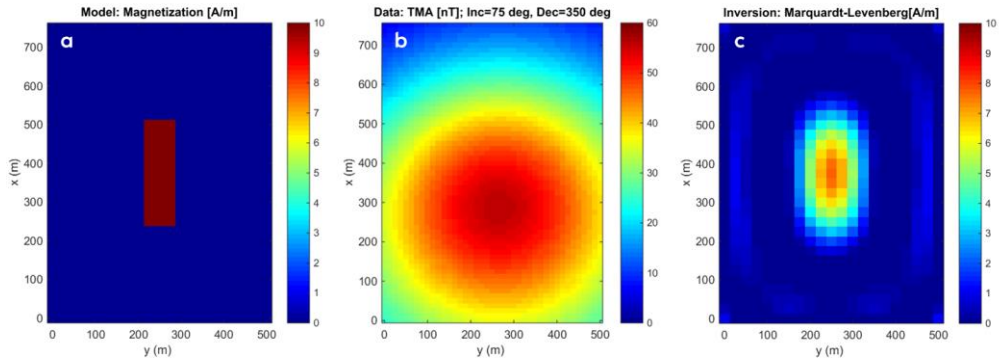

Figure 2: Synthetic magnetic inversion example. (a) Magnetic anomaly of $\mathbf{M = 10}$ A/m buried at a depth of 100m. (b) Modeled magnetic anomaly data. (c) Magnetization from inversion with the Marquardt-Levenberg method. The background field is $\mathbf{B_0 = 51000}$ nT. The inclination and declination are 75 degrees and 350 degrees, respectively.

Figure 2 shows a demonstration of the magnetic inversion on a simple synthetic model. The magnitude of the background field B_0 is 51000 nT. The inclination and declination are 75 degrees and 350 degrees, respectively. Synthetic magnetic data are forward modeled and then inverted using the Marquardt-Levenberg method. It can be observed that only a smoothed version of the rectangular, anomalous magnetic body is recovered.

4. PHENOMENOLOGICAL MODEL FOR ROCK MAGNETIZATION

Our next objective is to obtain a phenomenological model relating magnetization to underlying rock properties. In particular, a forward model $M(T)$ is needed for the likelihood part of the posterior distribution in equation 3. It's assumed that the forward model can be applied locally. The magnetic properties of rocks are mainly determined by a small number of strongly magnetic minerals. Most important are titanomagnetite, which may subsequently oxidize to titanomaghemite (Xu et la., 1997). Still, titanomagnetite only makes up a relatively small fraction of the total rock volume, typically 1-10%. The remanent and induced magnetization depend strongly on temperature, in addition to chemical processes and hydrothermal alteration. When magma cools and solidifies, single-phase titanomagnetite forms as a solid solution of magnetite and ulvöspinel. Upon further cooling, this solid solution may enter the miscibility gap, where it becomes unstable, and decomposes into new phases with different compositions.

To describe the thermal effects on magnetization, we want a simple model that links quantum effects to the macroscopic magnetization. Here we use the 1D Ising (1925) model from quantum statistics. In the Ising model, the Hamiltonian ε (energy) for a system of particles with interacting spins σ_j and under the influence of an external magnetic field H is given by

$$\varepsilon = -J \sum_{<ij>} \sigma_i \sigma_j - \mu_B H \sum_j \sigma_j , \tag{20}$$

where μ_B is the magnetic moment of each particle, J is the inter-particle interaction strength, and the notation $< ij >$ means that the sum runs over all nearest-neighbor combinations of. In equation 20, the first term represents remanent magnetization, and the second term induced magnetization.

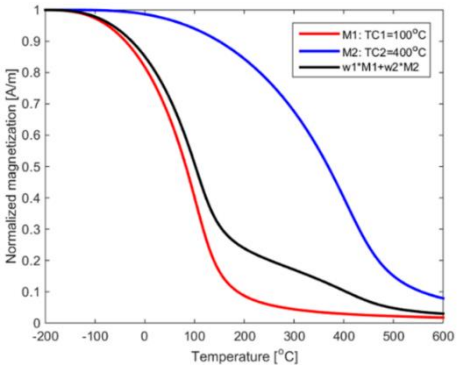

Figure 3: Two Ising models with different Curie temperatures $T_{C1} = 100$ °C (red) and $T_{C2} = 400$ °C (blue), and superposition of the two models (black).

After some algebra, using methods of statistical mechanics and the Boltzmann distribution, the macroscopic magnetization of a large ensemble of particles can be written as

$$\frac{M}{M_0} = \tanh\left[\frac{T_C M}{T M_0} + \frac{CH}{T M_0}\right], \tag{21}$$

where M is the magnitude of the magnetization, M_0 is the magnetization at absolute zero, T is the temperature (in Kelvin), T_C is the Curie temperature, and C is the Curie constant. Equation 21 is a transcendental equation which can be solved graphically or numerically. The susceptibility is given by

$$\chi = \frac{M(T,H) - M(T,0)}{H}, \tag{22}$$

where $M(T,0) = M_R$ is the remanent magnetization. For high temperatures, equation 21 can be linearized, which leads to the familiar Curie-Weiss law

$$\chi \simeq \frac{C}{T - T_C}. \tag{23}$$

The Ising model can be used to represent the magnetic properties of a homogeneous single-domain magnetic phase. We approximate a heterogeneous mix of magnetic phases, by a linear combination of single-phase models,

$$M(T,H) = \sum_j w_j M_j(T,H) , \tag{24}$$

where w_j is the weight of phase j. The linear superposition is supported by the linearity in magnetization of equations 4 and 10.

With equation 21 we can only model positive magnetization. Negative remanent magnetization (Nagata et al., 1952) is, sometimes observed in magnetic data, also for young MORB. Negative magnetization can be modeled by means of self-reversal for one or more

of the magnetic phases. In practice this can be achieved by means of negative weight w_j, and reversing the sign of H in equation 21. The model given in equation 24 can represent a large variety of temperature dependent magnetizations, by superposition of 2 or 3 mechanisms with different Curie temperatures (Figure 3), similar to experimental studies, e.g. as presented by Dietze et al. (2010).

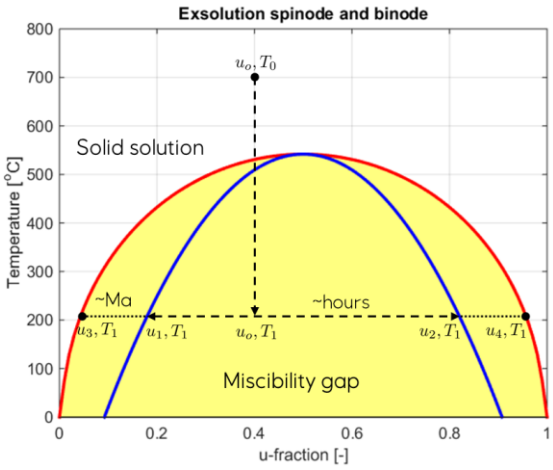

Figure 4: Exsolution binode $\frac{\partial G}{\partial u} = 0$ (red) and spinode $\frac{\partial^2 G}{\partial u^2} = 0$ (blue). The yellow area marks the miscibility gap. See main text for explanation.

When an igneous rock forms by cooling of magma, titanomagnetite forms as a solid solution of ulvöspinel and magnetite (Smith, 1980). Also, a part of the titanomagnetite may be transformed by high temperature oxidation to titanomaghemite (Xu et al., 1997). When the rock cools, solid exsolution takes place as follows (Figure 4): Assume that a homogeneous phase solid solution is formed at temperature T_0 with initial fractions u_0 and v_0 of the two compounds. Upon subsequent cooling to temperature T, the solid solution enters the miscibility gap, where it becomes unstable. and decompose by spinodal decomposition, into new phases with compositions u_1, v_1 and u_2, v_2. The phases may continue to decompose by binodal decomposition to phases with compositions $u_3, v_3$and u_4, v_4, however this relies on nucleation, associated with an activation energy, and is a much slower process (Yund and McAllister, 1969; Farjas and Roura, 2006; Wise et al., 2011). From mass conservation u and v are not independent, and the system can be described by one of them. In the following, we will use u.

For young, fast-cooling lavas, the spinodal decomposition is the relevant mechanism (Smith, 1980). The spinodal decomposition is controlled by the Gibbs free energy. For the simplest model, the Gibbs free energy and spinodal are symmetric around $u = 1/2$, as in the conceptual picture in Figure 4. Laboratory studies on spinodal decomposition of titanomagnetites by Wise et al. (2011), shows that the spinodal does not have this symmetry. Gibbs free energy for a two-component solution consists of an enthalpy term and an entropy term (Miracle and Senkov, 2017). In an external magnetic field, the entropy of the magnetite will be lower than the entropy of ulvöspinel, because magnetite is magnetic, whereas ulvöspinel is not. This asymmetry can be captured if we express the Gibbs free energy G of the system as (Figure 5)

$$\mathrm{G(u,v,T)} = \mathrm{W(uv + u\delta + v\delta)} + \mathrm{k_B T[(1+h)u\,lnu + (1-h)v\ln v + \delta\ln\delta]}, \tag{25}$$

*wh*ere u is the fraction of magnetite, v is the fraction of ulvöspinel, and δ is the fraction oxidized to titanomaghemite. We assume δ to be small, and constant during the spinodal decomposition. By mass conservation, we then obtain the condition $u + v + \delta = 1$ and $\partial \mathrm{u}/\,\partial \mathrm{v} = -1$. Moreover, W is the mixing-enthalpy parameter, $\mathrm{k_B}$ is the Boltzmann constant, and the parameter h accounts for the different magnetic entropies of magnetite and ulvöspinel in the presence of an external magnetic field.

The first and second derivatives of the Gibbs free energy are obtained as

$$\frac{\partial \mathrm{G}}{\partial \mathrm{u}} = -\mathrm{W(u-v)} + k_B \mathrm{T[(1+h)ln\,u - (1-h)\ln v + 2h]}, \tag{26}$$

$$\frac{\partial^2 \mathrm{G}}{\partial \mathrm{u}^2} = -2\mathrm{W} + \mathrm{k_B T}\left[\frac{(1+\mathrm{h})}{\mathrm{u}} + \frac{(1-\mathrm{h})}{\mathrm{v}}\right]. \tag{27}$$

The spinodal decomposition takes place when $\frac{\partial^2 \mathrm{G}}{\partial \mathrm{u}^2} < 0$, and terminates at the spinode defined by $\frac{\partial^2 \mathrm{G}}{\partial \mathrm{u}^2} = 0$ (Yund and McAllister, 1969). Equation 27 is a square equation for u, which gives two solutions u_1 and u_2, for two different solid solutions with different magnetite and ulvöspinel fractions. Setting $\mathrm{h} = 0$ and $\delta = 0$, a spinodal symmetric around $u = 1/2$ is obtained (Figure 4). The parameters W and h were adjusted to fit the spinodal model to the experimental measurements of Wise et al. (2011). Given temperature, the model then predicts the equilibrium fractions of ulvöspinel and magnetite for the phases with composition u_1 and u_2, respectively (Figure 5b). Moreover, from the empirical model presented by Lattard et al. (2006),

$$\mathrm{T_C(u)} = -150\mathrm{u}^2 - 580\mathrm{u} + 851, \tag{28}$$

we also obtain the corresponding Curie temperatures of the two phases (Figure 5b). By stoichiometric balancing, we obtain the weight functions for the Ising model in equation 24.

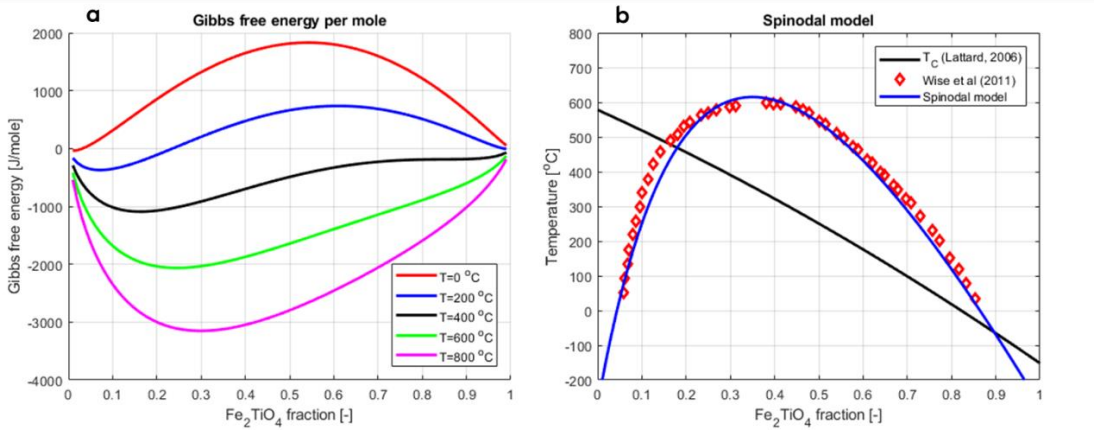

Figure 5: (a) Gibbs free energy as function of ulvöspinel fraction for various temperatures. (b) Model spinode (blue) calibrated to experimental results for titanomagnetite (red diamonds) presented by Wise et al. (2011). Also shown is the Curie temperature T_C of titanomagnetite (black) published by Lattard et al. (2006).

Because of the low depth resolution of magnetic potential field data, we have chosen a simplified representation in terms of depth-average magnetization, as given in equation 7. Consequently, we also seek a simplified parameterization for subsurface temperature vs depth. We represent the subsurface temperature T as

$$T(z, \beta) = T_\infty + (T_S - T_\infty)e^{-\beta z}. \tag{29}$$

where T_S is the land-surface temperature, and T_∞ is the asymptotic value for $z \to \infty$. With the decay parameter β varying from 0.1 to 0.5 km^{-1} we can then represent anything from conductive thermal gradients of order 40 °C/km to geothermal anomalies close to the boiling curve. The land-surface temperature T_S may vary significantly in active geothermal areas, e.g. near hot springs and fumaroles.

The land-surface temperature can be constrained on remote-sensing satellite data. Here we apply a method utilizing LANDSAT-8 bands 4, 5 and 8, i.e. the red, near infrared (NIR) and thermal infrared (TIRS) bands. We have adapted the method of Avdan and Jovanovska (2016) to a statistical inversion framework, similar to that presented for magnetization above. The resolution of the TIRS bands (90m) is however not able to capture the locally high temperatures near hot springs.

The decay parameter β can be associated with an average temperature $\hat{T}(\beta)$ defined by

$$\hat{T}(\beta) = \frac{1}{z_2 - z_1}\int_{z_1}^{z_2} T(z, \beta)dz. \tag{30}$$

Given average magnetization from inversion of magnetic anomaly data, we invert the average magnetization for average subsurface temperature of the magnetic source layer. Using equations 29 and 30, the link between average temperature and temperature vs depth is established at the forward modeling stage of the Bayesian inversion, i.e. as part of computing the likelihood part of the posterior probability distribution.

5. APPLICATION TO MAGNETIC DATA FROM REYKJANES, SOUTHWEST ICELAND

The methodology presented above was applied to magnetic line-data acquired at the Reykjanes geothermal field, in Southwest Iceland (Figure 6). The Reykjanes high temperature system is located at the boundary where the submarine Reykjanes Ridge meets the rift zone of southwest Iceland. This rift zone is highly permeable and is spotted with numerous fumaroles and hot springs at the surface. The spreading rate is approximately 2 cm/yr, and constitutes a slow-spreading zone.

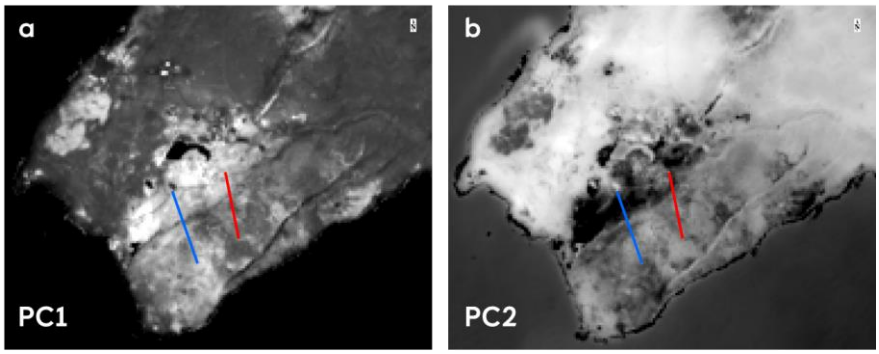

Figure 6: Location of magnetic Profile 3 (red) and Profile 5 (blue) shown on LANDSAT-8 satellite imagery, (a) PC 1 and (b) PC 2 from principle component (PC) analysis of the near infrared (NIR), short wave infrared (SWIR) and thermal infrared (TIR) channels (bands 5, 6, 7, 10 and 11). The extent of the Reykjanes geothermal area can be identified in the central part of the images. The processing of the satellite data was performed with the ENVI software.

The Reykjanes geothermal system can be considered a black-smoker analogue exposed on land (Friðleifsson et al., 2018). A geothermal powerplant with two turbines and 120 MWe electricity production is operated by HS Orka. The geology exposed at the surface is characterized dominantly by Holocene postglacial and historic extrusive basalts. The youngest lava in the northwest part of Reykjanes erupted in 1226. The lavas at the southeast side is covered by Skalafell lavas, 3000-8000 years old (Fridleifsson and Albertsson, 2000). The rocks investigated here belong to the youngest Holocene unit and formed as sub-areal basaltic lavas.

The basalts in the Reykjanes area are strongly magnetized with large remanence. Lateral variations are significant. Dietze et al. (2010) reported remanent magnetization varying from 0.1 to 20 A/m, and with Königsberger ratios Q>40 in feeder dykes and fissure eruptions. The young lavas at Reykjanes show significantly higher magnetization than Tertiary lavas other places in Iceland (Kristjansson and Jonsson, 2007). An aeromagnetic survey with flight altitude of 150 m revealed magnetic lows, which coincide with the center of the Gunnuhver hot spring and geothermal system at Reykjanes, with surface temperatures of up to 100 °C (Dietze et al., 2010).

Two densely sampled magnetic profiles, named Profile 3 and Profile 5, were acquired near the Reykjanes Geothermal field (Figure 6). The data was acquired on foot, using a GEM Systems GSM-19T Proton magnetometer. The length of each profile was approximately 1 km, with 12.5m between measurement locations. Only the scalar magnitude of the total magnetic intensity was measured. Surface susceptibility was measured in unvegetated areas with and Exploranium KT-9 Kappameter. The profiles were acquired on Skalafell lavas (3-8 ka). Measurements from the nearby Leirvogur Magnetic Observatory were used to correct for the Earth's magnetic background field, including diurnal variations, to obtain scalar magnetic anomaly data, as defined in equation 6. There is no clear correlation between the measured surface-rock susceptibility and magnetic anomaly data from co-incident locations (Figure 7). Low-pass filtered data shows a trend of increasing magnetization away from the core of the geothermal area (Figure 8).

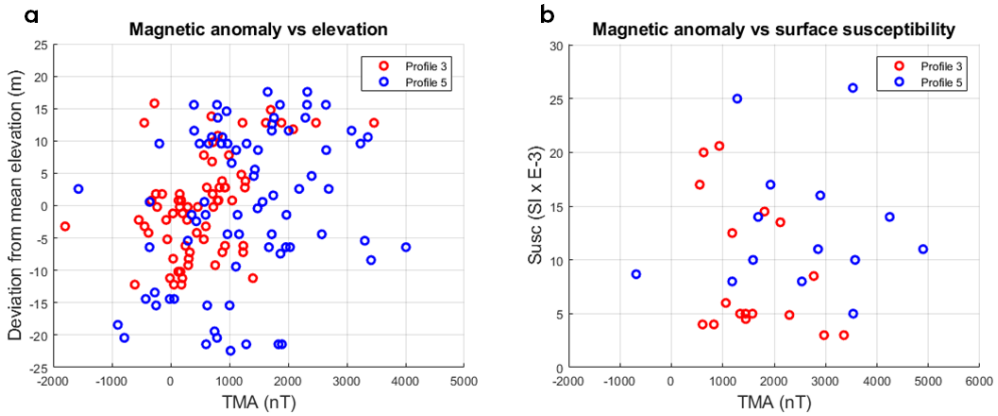

Figure 7: (a) Magnetic anomaly vs surface elevation along the profiles. (b) Magnetic anomaly vs surface-rock susceptibility measured on the parts of the profiles not covered by vegetation.

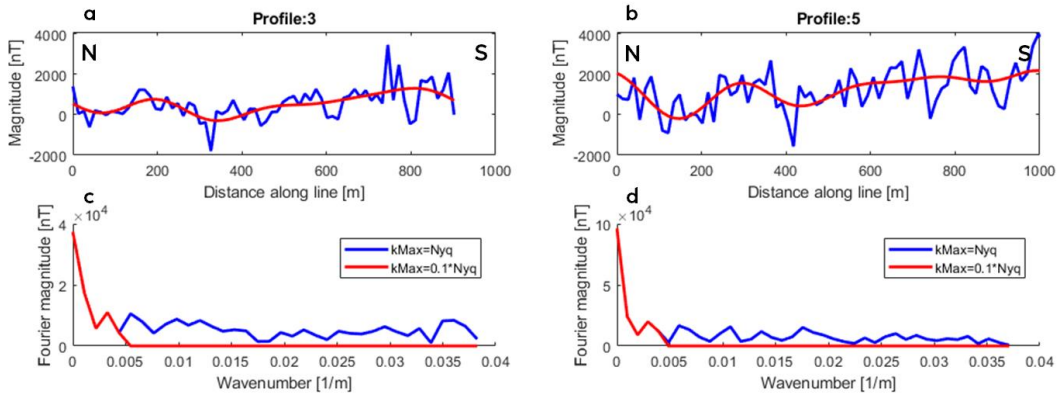

Figure 8: (a) and (b) Recorded magnetic anomaly data (blue) and low-pass filter trend (red) for Profile 3 and Profile 5, respectively. (c) and (d) The wavenumber spectra of the recorded and low-pass filtered magnetic anomalies. Profile 3 runs north to south, away from the geothermal area. Profile 5 runs south to north, towards the geothermal area.

Magnetization was computed using the Marquardt-Levenberg inversion scheme, as presented in equations 13 to 19 above. The magnetic field decays as $1/r^3$ (equations 4 and 12). Therefore, with measurement 2.5 m above the lava surface, the data will be dominated by near-surface magnetization. The depth sensitivity of the data was estimated using the wavenumber spectral method presented by Hsieh et al (2014), giving approximately180-230 m. This is in fair agreement with the modeling study of Dietze et al. (2010). Also, a sensitivity test using inversion was performed. In the inversions presented here, an effective source-layer thickness of $z_2 - z_1 = 200$ m was used (equation 7). The data input to the inversion were filtered with a 3-point moving average filter to attenuate random noise.

The magnetization obtained from the magnetic anomaly inversion was then input to the second stage of Bayesian inversion for temperature, computing the posterior distribution as defined in equations 1 and 3. It was assumed that forward model for the temperature-dependence of the magnetization (equations 21 to 27) can be applied locally (Hokstad et al., 2017). Given the posterior distribution, the mean and variance of the temperature is readily obtained. Co-rendering the inversion results with faults mapped on the surface (ISOR), indicates that anomalies are correlated to faults confined by fault segments (Figure 10).

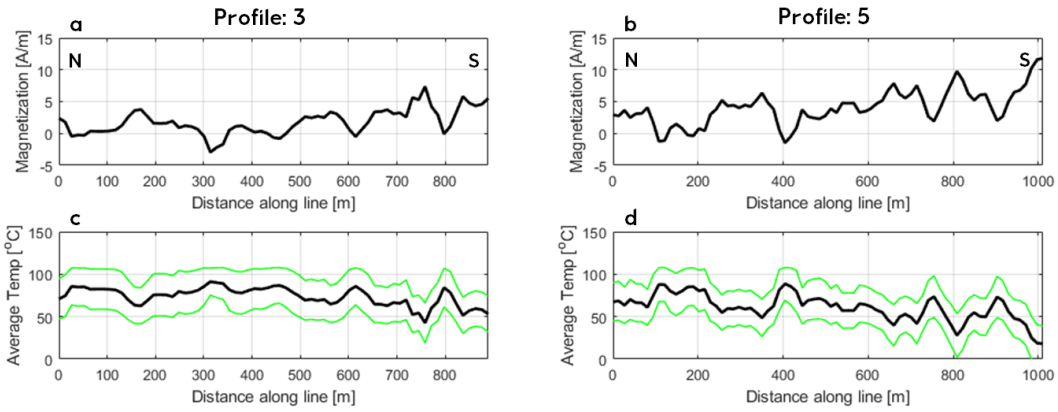

Figure 9: (a) and (b) Average magnetization from inversion of magnetic data along Profile 3 and Profile 5. (c) and (d) Posterior mean temperature (black) and variance (green) from Bayesian inversion of magnetization. Lines are plotted north-to-south.

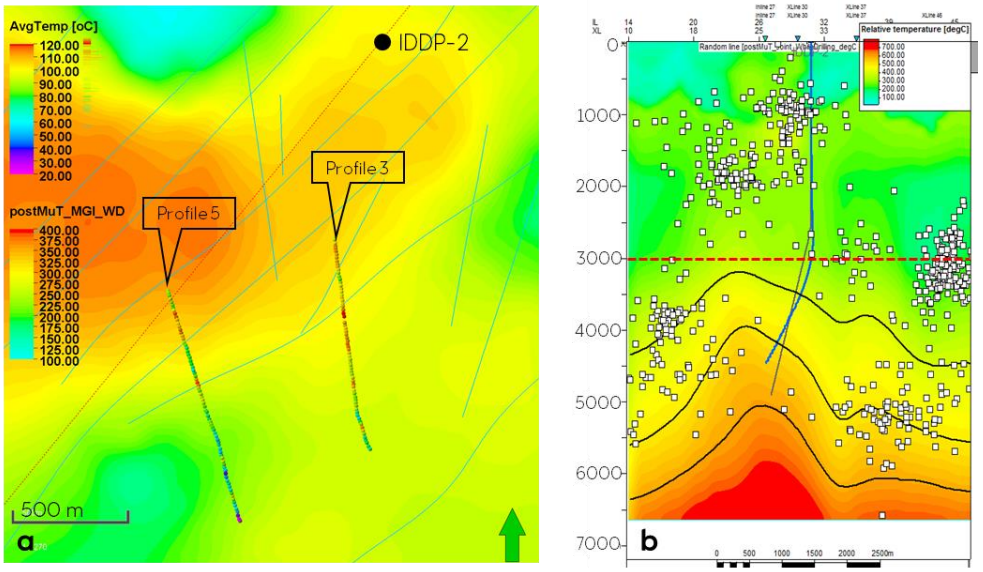

Figure 10: (a) Temperature prediction along Profile 3 and Profile 5 from Bayesian inversion, co-rendered with faults (green lines) mapped on the surface, and horizontal section at 300m depth from the 3D temperature prediction by Hokstad and Tänavsuu-Milkeviciene (2017) (b) Vertical section from the 3D temperature cube indicating the depth (red dashed line) of the horizontal section in (a).

Due to the limited depth resolution of magnetic data, the primary output from the two-stage inversion is magnetization and temperature averaged over the magnetic source layer. The depth-averaged temperature can then be associated with a temperature vs depth trend using the parametric representation given in equations 29 and 30 (Figure 11). Without well calibration, and with an assumption regarding the depth sensitivity of the magnetic measurements (200m in our case), we do not have control on the absolute magnitude of the estimated subsurface temperatures. However, relative lateral changes can be interpreted from the inversion results.

Based on results from the magnetic inversion and the temperature cube presented by Hokstad and Tänavsuu-Milkeviciene (2017), a 3D magnetic model for Reykjanes was constructed. The synthetic model was adjusted locally to reproduce approximately the magnetic data acquired along Profile 3 and Profile 5 (Figure 12). The purpose of this model was to test the influence of the acquisition altitude and to compare the modelled magnetic anomaly calculated at various heights to the data measured on the ground (solid line in Figure 12 b and c). We simulated flight altitudes from 5 to 250 m. The modeling result indicates that a flight altitude of 5-20 m should be chosen to resolve details of the geothermal system. Also, long-lines should be acquired to capture the deep trends of the system.

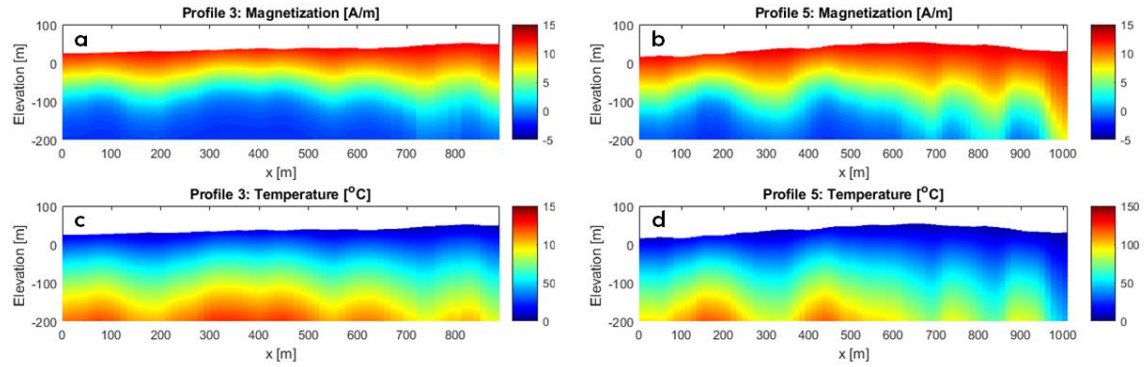

Figure 11: (a) and (b) Magnetization (c) and (d) Temperature. Vertical sections of Profile 3 and Profile 5, modeled using the depth-averaged magnetization and temperature from the Bayesian inversion.

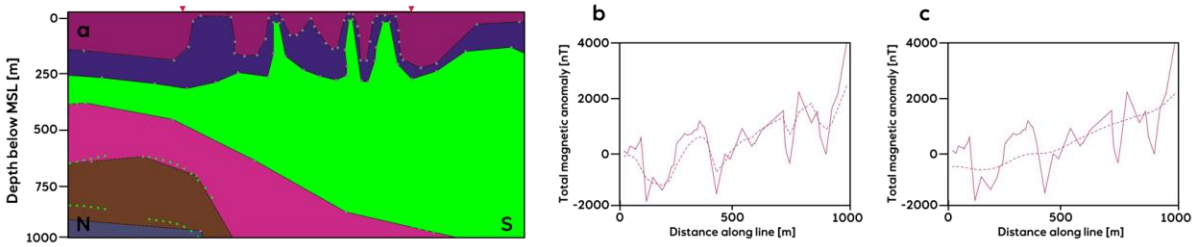

Figure 12: (a) Vertical section along Profile 5 from 3D magnetic model based on magnetization from inversion and 3D temperature cube in Figure 11. (b) and (c) Measured (solid) and modeled (dashed) total magnetic anomaly along Profile 5 with modeled recording level 10 m and 250 m above ground level, respectively. The start and end of Profile 5 is indicated by the red triangles in (a). The modeling was performed using the IGMAS software.

6. DISCUSSION AND CONCLUSIONS

We have proposed method for estimation of subsurface temperature from magnetic potential field data. The inversion method consists of two steps: (1) inversion of magnetic anomaly data for total magnetization, and (2) inversion of magnetization for temperature. The first step is a conventional magnetic potential field inversion. Due to the lack of depth sensitivity, we used a map-inversion method, inverting for average magnetization over a given depth range. However, in general, any magnetic inversion method can be applied, e.g. the method of Li and Oldenburg (1996) or Hokstad et al. (2017). For geothermal application in a basaltic setting, including both induced and remanent magnetization is important. This is feasible for young igneous rocks that have been crystalized approximately in the present-day magnetic background field, and close to the present position. Holocene rocks approximately fulfill this requirement, which has been assumed here. For old rocks, the location on Earth during formation, subsequent deformation, and knowledge of paleomagnetic field direction must be known.

The second inversion step is a rock-physics inversion and relies on a theoretical model relating magnetization to temperature. We have constructed a phenomenological model combining the classical Ising model from quantum statistics, and a spinodal exsolution model. This is applicable to relatively young volcanic rocks in geologically active areas (Yund and McAllister, 1969; Wise et al., 2011). For very old igneous rocks, such as continental crust and cratons, a binodal exsolution model and JMAK kinetics (Farjas and Roura, 2006) should be considered. The phenomenological model contains a set of parameters that are not easily obtained, such as the initial Titanium-fraction of the lavas at the time of crystalization, and the total percentage of magnetic material in the subsurface. These parameters can be lumped together in empirical factors that must be calibrated for each case at hand. In the present study, we have considered a system with fast-cooling lavas and a small amount of high-temperature oxidation. Chemical alteration was approximated as a fixed deterministic parameter. Only the re-distribution between magnetite-rich and ulvöspinel-rich titanomagnetite was included in the dynamic part of the model. On-going research focus on improvement of the rock-physics inversion, to incorporate hydrothermal alteration and low-temperature oxidation (oxidation-exsolution), and a theoretically sounder representation of magnetic entropy.

The method was tested on two lines from the Reykjanes geothermal area in Southwest Iceland. We can discriminate relatively hotter from relatively cooler areas. To obtain reliable absolute subsurface temperatures, better calibration to one or more geothermal wells is needed. In the Iceland field test, magnetic data was acquired on foot, with the magnetometer carried close to the lava surface, to obtain data with high lateral resolution. For 3D production acquisition, more efficient acquisition methods are needed. We suggest the use of drone-borne magnetometers flown at optimal altitudes. With two flight altitudes, also magnetic gradient data can be obtained. In the present work, we have only considered scalar magnetic data, which is normally acquired. Magnetization is a vector, with complex dependency on present and paleo earth magnetic field. In general, to fully resolve the vector nature of the magnetization in the inversion, multicomponent measurement of the magnetic anomaly vector field is needed.

The proposed method may be useful in exploration for blind geothermal systems. Also, we believe it can be applied to relate small-scale shallow features to deep features and for geological model building of geothermal systems (Tänavsuu-Milkeviciene et al., 2018). Due to the inherent ill-posed nature of magnetic inversion, we do not consider it to be a standalone tool. Rather we will use the

proposed inversion scheme as part of multigeophysical inversion (Hokstad and Tänavsuu-Milkeviciene, 2017) and integrated geological and geophysical interpretations.

7. ACKNOWLEDGEMENTS

We thank Equinor for permission to publish this work, and HS Orka for permission to acquire magnetic data on their licensed acreage. Part of this research was supported by the EU H2020 project DEEPEGS Grant Agreement No 690771.

REFERENCES

Anderson, T.W., 1994, An introduction to multivariate statistical analysis: John Wiley and Sons.

Avdan, U., and G. Jovanovska, 2016, Algorithm for automated mapping of land-surface temperature using LANDSAT 8 satellite data: Journal of Sensors, **2016**, 1-8.

Bhattacharyya, B., 1964, Magnetic anomalies due to prism-shaped bodies with arbitrary polarizations: Geophysics, **4**, 29.

Blakely, R., 1996, Potential theory in gravity and magnetic applications: Cambridge University Press.

Buland, A., O. Kolbjørnsen, R. Hauge, Ø.Skjæveland, and K. Duffaut, 2008, Bayesian lithology and fluid prediction from seismic prestack data: Geophysics, **73**, C13-C21.

Cowell, R., P. Dawid, S. Lauritzen, and D. Spiegelhalter, 2007, Probabilistic networks and expert systems: Exact computational methods for Bayesian networks, in Statistics for engineering and information science series: Springer.

Dietze, F., A. Kotny, I. Heyde, and C. Vahle, 2010, Magnetic anomalies and rock magnetism of basalts from Reykjanes (SW-Iceland): Studia Geophysica et Geodaetica, **55**, 109-130.

Farjas, J., and P. Roura, 2006, Modification of the Kolmogorov-Johnson-Mehl-Avrami rate equation for non-isothermal experiments and its analytical solution: Acta Materialia, **54**, 5573-5579.

Friðleifsson G.Ó., and A. Albertsson, 2000, Deep geothermal drilling on the Reykjanes Ridge: opportunity for international collaboration: Presented at the World Geothermal Congress, Proceedings.

Friðleifsson, G.Ó., et al., 2018, The Iceland Deep Drilling Project at Reykjanes: Drilling into the root zone of a black smoker analog, J. Volcanol. Geotherm. Res

Hokstad, K., Tašárová, Z.A., Clark, S.A., Kyrkjebø, R., Duffaut, K., Fichler, C. & Wiik, T. 2017: Radiogenic heat production in the crust from inversion of gravity and magnetic data.. Norwegian Journal of Geology 97, 241–254. https://dx.doi.org/10.17850/njg97-3-04.

Hokstad, K., and K. Tänavsuu-Milkeviciene, 2017, Temperature prediction by multigeophysical inversion: Application to the IDDP-2 well at Reykjanes, Iceland: GRC Transactions, **42**, 1141- 1152.

Hsieh, H.-H., Chen, C.-H., Lin, P.-L., and Yen, H.-Y., 2014, Curie point depth from spectral analysis of magnetic data in Taiwan: J.Asian Earth Science, **90**, 26-33.

Ising, E., 1925, Beitrag zur theorie des ferromagnetismus: Z.Phys, **31**, 253-258.

Kristjansson, L., and G. Jonsson, 2007, Paleomagnetism and magnetic anomalies in Iceland: J. Geodynamics, **43**, 30-54.

Lattard, D., R. Engelmann, A. Kontny, and U. Sauerzapf, 2006, Curie temperatures of synthetic titanomagnetites in the Fe-Ti-O system: Effects of composition, crystal chemistry, and thermomagnetic methods: J. Geophys. Res., **111**.

Li, Y., and D. Oldenburg, 1996, 3-D inversion of magnetic data: Geophysics, **61**, 394-408.

Lilleborge, M., R. Hauge, and J. Eidsvik, 2015, Information gathering in Bayesian networks applied to petroleum prospecting: Mathematical Geosciences, **48**, 233-257.

Miracle, D., and O. Senkov, 2017, A critical review of high entropy alloys and related concepts: Acta Materialia, **122**, 448-511.

Nagata, T., S. Uyeda, and S. Akimoto, 1952, Self-reversal of thermo-remanent magnetism of igneous rocks: J. Geomag and Geoelectricity, **4**, 22-38.

Smith, P., 1980, Spinodal decomposition in a titanomagnetite: American Mineralogist, **65**, 1038- 1043.

Stacey, F., 1974, The physical principles of rock magnetism: Elsevier.

Tänavsuu-Milkeviciene, K., K. Hokstad, I. Merciu, and C. Kruber, 2018, Understanding geothermal reservoirs: IDDP-2, Iceland: Presented at the AAPG GTW Series, Proceedings.

Vine, F., and D. Matthews, 1963, Magnetic anomalies over oceanic ridges: Nature, **199**, 947-949.

Wise, A., M. Saenko, A. Valazquez, D. Laughlin, M. Daiz-Michelena, and M. McHenry, 2011, Phase evolution in the Fe_3O_4-Fe_2TiO_4 pseudo-binary system and its implications for remanent magnetization in martian minerals: IEEE Transactions on Magnetics, **47**, 4124-4127.

Xu, W., D. Peacor, W. Dollase, R. Van Der Voo, and R. Beaubouff, 1997, Transformation of titanomagnetite to titanomaghemite: A slow, two-step, oxidation-ordering process in MORB: American Mineralogist, **82**, 1101-1110.

Yund, R., and R. McAllister, 1969, Kinetics and mechanisms of exsolution: Chemical Geology, **6**, 5-30.